ELSEVIER

Contents lists available at ScienceDirect

Applied Catalysis B: Environmental

journal homepage: www.elsevier.com/locate/apcatb



Surface-catalyzed hydrolysis by pyrogenic carbonaceous matter and model polymers: An experimental and computational study on functional group and pore characteristics



Zhao Li ^a, Ryan Jorn ^b, Pamela Rose V. Samonte ^a, Jingdong Mao ^c, John D. Sivey ^d, Joseph J. Pignatello ^e, Wenqing Xu ^{a, *}

- ^a Department of Civil and Environmental Engineering, Villanova University, Villanova, PA 19085, USA
- ^b Department of Chemistry, Villanova University, Villanova, PA 19085, USA
- ^c Department of Chemistry and Biochemistry, Old Dominion University, Norfolk, VA 23529, USA
- ^d Department of Chemistry, Towson University, Towson, MD 21252, USA
- e Department of Environmental Sciences, The Connecticut Agricultural Experiment Station, 123 Huntington St., New Haven, CT 06511, USA

ARTICLE INFO

Keywords: Pyrogenic carbonaceous matter Nanopore characteristics Base catalysis Quaternary ammonium groups Molecular dynamics modeling

ABSTRACT

We employed a polymer network to understand what properties of pyrogenic carbonaceous matter (PCM; e.g., activated carbon) confer its reactivity, which we hereinafter referred to as PCM-like polymers (PLP). This approach allows us to delineate the role of functional groups and micropore characteristics using 2,4,6-trinitro-toluene (TNT) as a model contaminant. Six PLP were synthesized via cross-coupling chemistry with specific functionality (-OH, -NH₂, -N(CH₃)₂, or -N(CH₃)^{\pm}) and pore characteristics (mesopore, micropore). Results suggest that PCM functionality catalyzed the reaction by: (1) serving as a weak base (-OH, -NH₂) to attack TNT, or (2) accumulating OH near PCM surfaces (-N(CH₃) $^{\pm}$). Additionally, TNT hydrolysis rates, pH and co-ion effects, and products were monitored. Microporous PLP accelerated TNT decay compared to its mesoporous counterpart, as further supported by molecular dynamics modeling results. We also demonstrated that quaternary ammonium-modified activated carbon enhanced TNT hydrolysis. These findings have broad implications for pollutant abatement and catalyst design.

1. Introduction

Pyrogenic carbonaceous matter (PCM) refers to the pyrolysis products of fresh or fossilized biomass, including environmental black carbon (e.g., fossil fuel soot and chars) and engineered carbons (e.g., graphene, biochar, and powdered activated carbon (PAC)) [1,2]. Traditionally, PCM is considered a passive adsorbent for binding pollutants or providing microbes with an inert surface to grow [3–9]. Recently, a small but growing body of literature reports that PCM is intrinsically reactive and can participate in various reactions critical to biogeochemical processes [10–12], climate change [13,14], and contaminant transformation [15–19]. However, the properties of PCM that confer its reactivity remain unclear in most cases. Although PCM is ubiquitous in the environment, the concentration, redox status, and surface properties of PCM that may affect its reactivity vary significantly, depending on source material, formation conditions, aging, and the environment in

which it is found. The inherent heterogeneity of the PCM-system thus makes it difficult to predict the degree of contaminant transformation occurring in both natural and engineered environments. To define the conditions necessary for desired reactions to occur, we need to delineate the contributions of individual properties of PCM that are relevant.

Functional group identity and pore characteristics are two such relevant properties. PCM is an amorphous porous solid containing micropores (<2 nm), mesopores (2–50 nm; IUPAC definition), and macropores [20,21], as well as oxygen and nitrogen functional groups [22–24]. Previous studies found that PCM can facilitate alkaline hydrolysis of nitroaromatic compounds (e.g., 2,4,6-trinitrotoluene (TNT), 2,4-dinitroanisole (DNAN)) and alkyl bromides (e.g., methyl bromide) [19,25,26]. Hydrolysis of TNT by PCM and methyl bromide even occurred at circumneutral pH [19,25,26]. These results have important implications for both *in-situ* and *ex-situ* contaminant clean-up. Efforts have been made to identify the PCM properties responsible for the

E-mail address: wenqing.xu@villanova.edu (W. Xu).

^{*} Corresponding author.

accelerated hydrolysis. Some studies suggest that surface functional groups such as $-\mathsf{OH}$ and $-\mathsf{NH}_2$ on activated carbon or carbon nanotubes can initiate conversion of 1,1,2,2-tetrachloroethane to trichloroethylene by base-catalyzed elimination of HCl [23,24]. Other studies proposed that the enhanced decay of TNT, DNAN, and alkyl bromides was due to an increased local concentration of the hydroxide ion (OH) near the surface of PCM [19,25,26]. In support, computational studies show accumulation of OH near the surface of graphene due to a balance between ion-surface and ion-water interactions [27,28].

Another feature of PCM that may be critical for its reactivity is its high microporosity [1]. Chemical reactions can be significantly accelerated within micropores due to the nanoconfinement effect [29–31]. Specifically, confined entities may exhibit different chemical and physical properties that lead to enhanced reactivity compared to the unconfined bulk phase [32,33]. For instance, higher catalytic performance was observed when metal or metal oxide nanoparticles were confined in carbon nanotubes [34,35], or when terminal alkyne and a palladium complex were encapsulated within a coordination cage [36]. A recent study observed a three order of magnitude enhancement in the acid-induced pollutant transformation rate when the nanoscale Mn_3O_4 catalyst particles were spatially confined in mesopores, which was attributed to the elevated local proton concentrations near the nanoparticle surface [37]. However, to date, the effect of PCM microporosity on contaminant transformation has received little attention [1].

One way to overcome the heterogeneity issue that hampers the direct mechanistic characterization of PCM reactivity is to employ PCM-like polymers (PLP) that have features resembling individual PCM attributes. The PLP exhibit properties that are similar to PCM: (i) large surface area and high microporosity, (ii) highly conjugated and amorphous, and (iii) superior affinity for apolar organic contaminants. Unlike PCM, the attributes of PLP can be individually tuned and made homogeneously throughout the polymer networks [38–40].

The goal of this study is to investigate the effect of PCM functionality and pore characteristics on contaminant hydrolysis by utilizing PLP. We selected TNT as a model contaminant because it has been previously demonstrated to undergo PCM-facilitated hydrolysis [25]. Surface functional groups (i.e., -OH, -NH₂, -N(CH₃)₂, -N(CH₃)₃⁺) were incorporated into PLP by adapting the synthesis approach described in our previous work [38]. The pore characteristics of PLP was controlled by rigid node-strut topology, where two polymers were obtained: one with exclusively mesopores vs. the other with a mixture of micropores and mesopores. The reactivity of each of the six synthesized PLP, powdered AC (PAC), and PAC adsorbed with a quaternary ammonium (QA) polymer was subsequently quantified by measuring the TNT decay rate. In selected samples, TNT kinetics under various pH conditions, the co-ion effect, and transformation product analyses were conducted. Lastly, molecular dynamics modeling was performed using graphene sheets that were both plain and decorated with -N(CH₃)⁺₃ groups to elucidate the reaction mechanism. Overall, this study is the first attempt to scrutinize the complex properties of PCM, namely the functional group identity and pore characteristics, responsible for promoting contaminant hydrolysis. The findings of the study have potentially broad implications for pollutant abatement and the design of catalysts.

2. Materials and methods

2.1. Chemicals and the activated carbon adsorbent

The chemicals used in PLP synthesis along with their source and purity are listed in the Supplementary Information (SI) section. TNT (1000 $\mu g \cdot mL^{-1}$ in acetonitrile) was obtained from Chem Service, Inc. (West Chester, PA). Deionized water (18.2 $M\Omega \cdot cm$) was obtained from a Millipore milli-Q-plus water purification system.

Poly-diallyldimethylammonium chloride (polyDADMAC), a QA

polymer, was non-covalently attached to powdered AC (PAC; Norit RO 0.8) by suspending PAC in aqueous polyDADMAC (20% by wt; Sigma Aldrich) for 24 h, filtering off the solid, and washing the recovered solid with clean water by the method detailed in [26]. The obtained PAC is abbreviated as Norit_RO_PD.

2.2. Synthesis of PCM-like polymers with various functionality and pore characteristics

Six PLP were synthesized by Pd(0)/Cu(I)-catalyzed cross-coupling chemistry following a method adapted from our previous study [38]. Four PLP with different surface functionalities were obtained, where PLP-OH, PLP-OH/-N+(CH3)3, PLP-NH2, and PLP-N(CH3)2 represent polymers with -OH, a mixture of -OH and -N⁺(CH₃)₃, -NH₂, and -N(CH₃)₂ groups, respectively. Details on the synthesis are summarized in the SI section. The synthesis routes for PLP-OH and PLP-OH/-N+(CH3)3 are shown in Scheme 1; the synthesis routes for PLP-NH2 and PLP-N(CH3)2 are shown in Scheme 2. Two PLP with different porosities were also obtained in this study, where PLP-micro represents polymers with a mixture of micropores (< 2 nm) and mesopores (2-50 nm), whereas PLP.meso stands for polymers with exclusively mesopores (2-50 nm). The synthesis routes for PLP-micro and PLP-meso are shown in Scheme 3. Briefly, 1, 4-diethynylbenzene (252 mg, 2.0 mmol), 2,5-dibromoaniline (502 mg, 2.0 mmol), tetrakis-(triphenylphosphine)palladium(0) (100 mg, 0.087 mmol), and copper(I) iodide (30 mg, 0.158 mmol) were dissolved in a mixture of N,N-dimethylformamide (10 mL) and triethylamine (10 mL) for 0.5 h under N2. The reaction mixture was stirred at 80 °C for 72 h under N₂ and kept in the dark [41]. After the reactor was cooled down to room temperature, the mixture was filtered by membrane filtration with 0.45 µm pore size (Whatman plc, Maidstone, UK). The dark yellow solids on the filter were collected and dried, which was abbreviated as PLP-micro. The light yellow solids was precipitated with methanol from the filtrate and abbreviated as PLP-meso. Subsequently, both PLP-micro and PLP-meso were washed with chloroform, followed by water, methanol, and acetone to remove the unreacted monomers and catalyst residues. Further purification of the polymer was carried out by Soxhlet extraction with methanol for 72 h and then dried at 70 °C for 24 h.

2.3. PCM-like polymer characterization

2.3.1. Infrared spectroscopy

Fourier transform infrared spectra (FTIR) were obtained on a Perkin Elmer 1600 Series FTIR Spectrophotometer. Each sample was scanned 32 times with a resolution of $4~\rm cm^{-1}$.

2.3.2. Solid-state NMR

Nuclear magnetic resonance (NMR) experiments were conducted on a Bruker Avance 400 spectrometer at 100 MHz ^{13}C frequency with 4-mm sample rotors in a double-resonance probe head. A previously established ^{13}C multiple cross-polarization/magic angle spinning (multi-CP/MAS) NMR technique was applied to collect quantitative structural information of PCM-like polymers [38,42] and further analysis was performed to study the degree of polymerization [43,44]. The spinning rate was at 14 kHz and the 90° pulse length was 4 μs for ^{13}C . The spectra exhibited good signal-to-noise ratios with rotating sidebands spun out of centerbands.

2.3.3. Electron microscopy

Scanning electron microscopy (SEM; Hitachi S-4800, TYO, Japan) and transmission electron microscopy (TEM; JEOL JEM-1400) were used to observe the morphologies of the synthesized PLP. The accelerated voltages for SEM and TEM were 3 kV and 100 kV, respectively.

2.3.4. Gas sorption analysis

Surface areas and pore size distributions were measured by nitrogen

Scheme 1. $\mbox{PLP}_{\mbox{-OH}}$ and $\mbox{PLP}_{\mbox{-OH/-N+(CH3)3}}$ synthesis routes.

Scheme 2. PLP-NH2 and PLP-N(CH3)2 synthesis routes.

$$= + Br \xrightarrow{NH_2} Br \xrightarrow{Pd, CuI} * \left(= - \frac{NH_2}{Et_3N, DMF} \right)^*$$

$$PLP_{-micro} and PLP_{-meso}$$

Scheme 3. PLP-micro and PLP-meso synthesis routes.

adsorption and desorption at 77.3 K using a NOVA 3000e (Quantachrome Instruments, Boynton Beach, FL, U.S.A.) from 0.0125 to 0.98 p/p₀. An equilibrium time of 1800 s was used. The samples were outgassed at 110 $^{\circ}\text{C}$ for 18 h under dynamic vacuum.

2.3.5. X-ray photoelectron spectroscopy

X-ray photoelectron spectroscopy (XPS) data acquisition was performed on a Versa Probe I instrument. Both survey and high-resolution spectra were acquired with a 200 $\mu m,~50$ W beam using 117 eV and 23 eV pass energies, respectively. Dual-source neutralization with a combination of ion gun and neutralization was used during analysis. Data was charge corrected to adventitious carbon 284.8 eV BE. Argon sputtering was employed to clean the surfaces and Ar+ 2kV2 μA were utilized for a period of 2 min for each dry powder sample placed on the sample holder.

2.4. Adsorption isotherm and kinetics experiments

The reactivity of PAC (*i.e.*, Norit D10, Norit_RO, Norit_RO_PD) and PLP was quantified by measuring their ability to accelerate TNT decay [25]. TNT stock solution (50 μL , 1000 mg·L $^{-1}$ in methanol) was spiked into borosilicate glass reactors containing pre-weighed solids (2.5 g·L $^{-1}$ for PCM-like polymers, Norit D10; 10 g·L $^{-1}$ for Norit_RO, Norit_RO_PD) over a range of pH conditions. A 10 mM buffer mixture containing chloride, phosphate, and carbonate was used to achieve and maintain the pH at 3, 5, 7, and 9. HCl was used to adjust the pH to 3. Experiments with Norit D10, Norit_RO, and Norit_RO_PD used either a 10 mM carbonate/bicarbonate (pH 10.0 \pm 0.2) or 10 mM citrate (pH 3.0 \pm 0.2) buffer mixture. All vials were capped with Teflon-lined septa and placed on a rotator in the dark at 30 rpm, 25 °C or 55 °C. Controls without solids were prepared at the same time. Adsorption kinetics with PLP,

following the same procedure, were performed at pH 3 to eliminate TNT alkaline hydrolysis. Experiments on the co-ion effect were performed with PLP $_{\rm NH2}$ (2.5 g·L $^{-1}$) at pH 9, where TNT was spiked in after the addition of 20 mM of KCl, KI, or Na $_2$ CO $_3$ /NaHCO $_3$. Experiments with Norit D10 were performed by 10 successive additions of TNT (250 μ M) to the experimental matrix every 24 h for a total of 10 days. All experiments were conducted in duplicate.

2.5. Chemical analysis

Replicate samples were collected periodically for analysis. Vials were centrifuged at 3000 rpm for 3 min to separate the aqueous and solid phases. Details on solvent extraction of the solids, chromatographic analysis of TNT (absorbance at 254 nm), colorimetric nitrite analysis (absorbance at 543 nm), and analysis of organic transformation products (UPLC, Waters Acquity H-Class with a high-resolution, quadrupole/time-of-flight (qTOF) mass spectrometer) are given in the SI. The solid phase extraction efficiencies from all PLP were > 80% (Table S1).

2.6. Molecular dynamics simulations

Further mechanistic insights were obtained by performing nonreactive molecular dynamics simulations on idealized pore structures. A force field model was selected for water and NaOH that provided reasonable electrolyte structure and solvation free energies. Water was represented by the SPC/E model [45] and the Lennard-Jones parameters for Na⁺, OH⁻, and Cl⁻ were taken from Bonthuis et al. [46]. The TNT molecule was described by the Consistent Valence Force Field (CVFF) developed for amino acid residues containing nitrogen functionalities [47]. Graphene sheets were arranged at varying distances of 1–4 nm to replicate a simple pore geometry for PCM. While the graphene sheets were frozen during the simulation, they interacted with the liquid electrolyte via the Lennard-Jones parameters for aromatic carbons from CVFF. After constructing the pores, the gap between the sheets was filled with electrolyte by random packing via Packmol [48].

The impact of surface functionalities on the electrolyte structure was also considered by adding QA groups (–N(CH $_3$) $_3^{\pm}$) to the plain graphite sheets at varying surface coverages from 1 to 9 groups per 565 Å 2 . With the addition of the positively charged surface groups, the system was kept charge neutral by adding compensating chloride ions (Cl $^-$). Concentrations of Cl $^-$ were comparable to those of sodium hydroxide (Figs. S7–S10), ranging from effectively 0.30–1.8 M in the confined pores. All simulations were carried out using the LAMMPS software package [49] within the NVT ensemble (Nose-Hoover thermostat) at 300 K. Periodic boundary conditions were employed along the x- and y-directions, with the confinement along the z-axis. The particles interacted via the Lennard-Jones (LJ) pair potential with a cut-off radius at 12 Å and the particle-particle particle-mesh method was used to compute the long-range Coulomb interaction. In all cases, the total density of water and ions was fixed at 1 g·cm $^{-3}$ and a timestep of 1 fs was chosen.

3. Results and discussion

3.1. Characterization of the synthesized PCM-like polymers

The chemical structures of the synthesized PLP were first verified by FTIR spectroscopy (Fig. 1). The disappearance of terminal alkyne (3293 cm $^{-1}$, \equiv C-H stretch) coupled with the presence of quaternary alkyne (2180 cm⁻¹, R-C\(\exists C-R'\) stretch) were observed in all PLP [50], indicating that cross-coupling between aryl halide and terminal alkyne was successful. Furthermore, the presence of a phenolic peak (3521 cm⁻¹, O-H stretch) and primary amines (3470 cm⁻¹ and 3378 cm⁻¹, N-H stretch) in PLP_{-OH} and PLP_{-NH2} spectra, respectively, confirmed the successful incorporation of these functional groups into PLP. The peaks at 1107 cm⁻¹ and 2835 cm⁻¹ in PLP_{-OH/-N+(CH3)3} and PLP-N(CH3)2 spectra could be ascribed to aliphatic ether (C-O-C) and methyl (C-H) groups, respectively, due to further modification of PLP-OH and PLP-NH2. Compared to PLP-NH2, PLP-micro and PLP-meso were synthesized by altering the node that is notionally linear rather than cross-linked. Nonetheless, the infrared spectra of these three samples (PLP $_{\text{-NH2}}$, PLP $_{\text{-micro}}$, and PLP $_{\text{-meso}}$) were similar and showed two main wavenumber regions: primary amine stretching in the 3100–3500 cm⁻¹ regions confirm the incorporation of -NH₂, whereas benzene ring

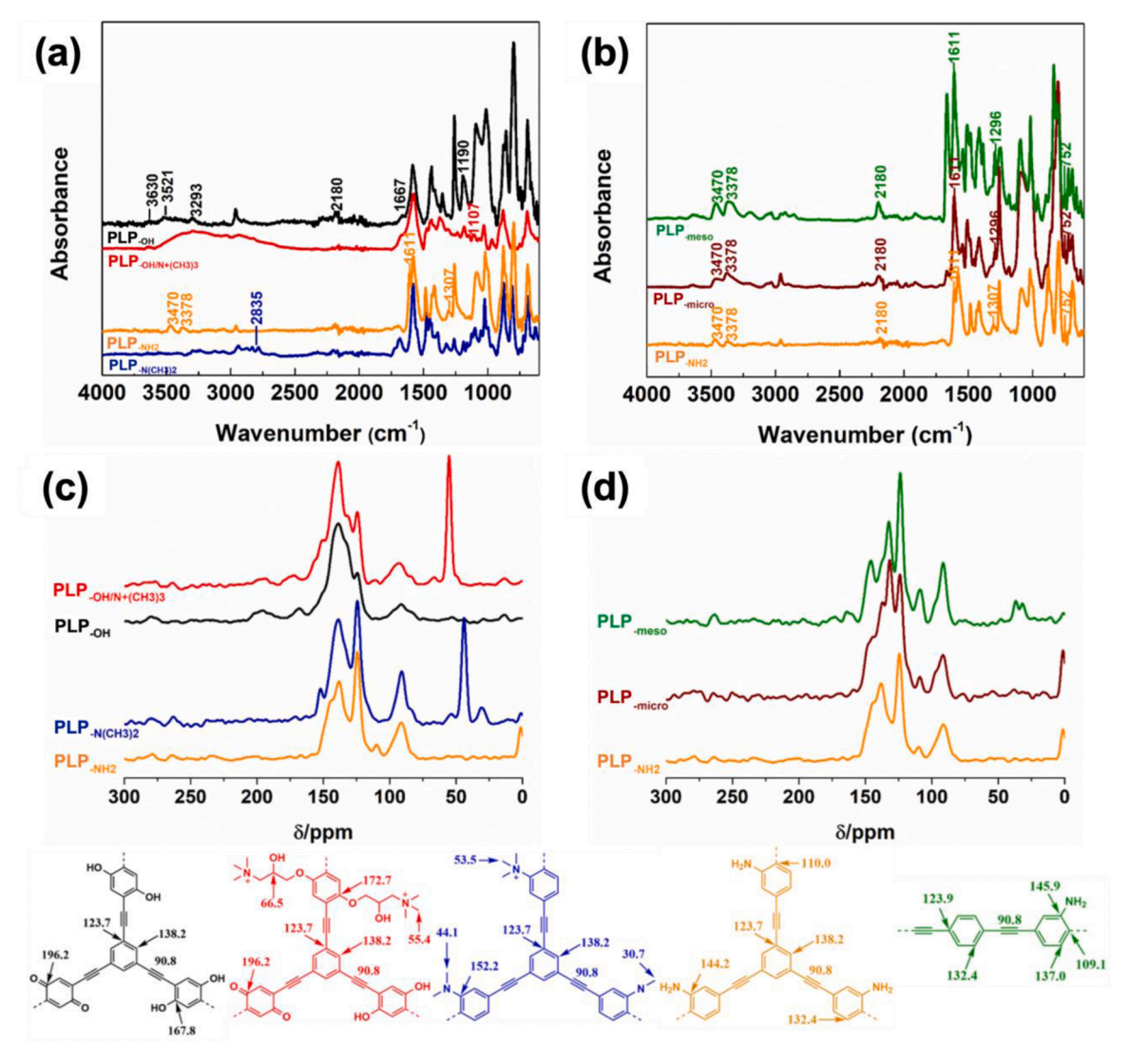


Fig. 1. (a) FTIR spectroscopy of PLP_{-OH} , $PLP_{-OH/-N+(CH3)3}$, PLP_{-NH2} , and $PLP_{-N(CH3)2}$. (b) FTIR spectroscopy of PLP_{-NH2} , PLP_{-micro} , and PLP_{-meso} . (c) Solid state ^{13}C multiCP/MAS NMR spectrum and peak assignments of $PLP_{-OH/-N+(CH3)3}$, PLP_{-NH2} , and $PLP_{-N(CH3)2}$. (d) Solid state ^{13}C multiCP/MAS NMR spectrum and peak assignments of PLP_{-micro} , and PLP_{-micro} , and PLP_{-micro} . All spectra were recorded at a spinning speed of 14 kHz with a 90° ^{13}C pulse-length of 4 μ s.

skeleton vibration in $1400-1650 \text{ cm}^{-1}$ confirms the aromatic skeleton in the polymer network. Details on peak assignment are summarized in Table S2.

To understand the chemical structures of the polymer networks at a molecular level, we characterized these polymers using $^{13}\mathrm{C}$ multi-CP/ MAS solid-state NMR (Fig. 1c and d). In all spectra, the skeleton of polymer networks and the peaks of PLP-OH were consistent with previously reported values [38]. Briefly, the incorporation of chemical functionalities in the framework and efficient coupling between aryl halides and alkyne were observed. As shown in Fig. 1c, the peak at 55.4 ppm in the PLP $_{\rm OH/-N+(CH3)3}$ spectrum can be ascribed to the carbon in methyl groups attached to QA ($C_{N+-(CH3)3}$). Moreover, loss of the amine resonance at 144.2 ppm ($C_{Ar\text{-}NH2}$) in the PLP- $_{NH2}$ spectrum and the presence of additional peaks at 152.2 ppm (CAr-N(CH3)2) in the PLP-N (CH3)2 spectrum suggest the successful methylation of primary amine by methyl iodide. Notably, the peak at 44.1 ppm (C_{N-(CH3)2}) suggests that the reaction of PLP._{NH2} with methyl iodide yields mostly tertiary amines. This can be explained by the effect of steric hindrance on the reaction and the possibly slow diffusion of the methylating agent into polymer pores [51,52], resulting in mostly tertiary amine groups rather than quaternary amine. As shown in Fig. 1d, the resonances at 132.4 ppm in both PLP-micro and PLP-meso spectra confirmed the incorporation of 1, 4-diethenylbenzene as a node in the polymer network. Moreover, the terminal junction of the strut (CAr-Br, 109.1 ppm) provided clear evidence of the unreacted aryl halides. The ratio of the peak at 80.3 ppm (C-C=C-H) over the peak at 90.8 ppm (C_{R-CC-R'}) suggests that PLP-micro (0.28) has a higher condensation degree than PLP-meso (0.32). Details on peak assignment are summarized in Table S3. Additional solid state ¹³C NMR analysis was performed to quantify the percentages of carbon bonded to the surface functional groups in the PLPs. Of the six PLPs, the amount of surface functional groups ranged from 1.42% to 4.98% (Table S4; Fig. S1).

The morphology of PLP. $_{\rm micro}$ and PLP. $_{\rm meso}$ was investigated by SEM and TEM. The SEM image of PLP. $_{\rm NH2}$ (Fig. 2a) showed a fluffy porous structure, suggesting a porous three-dimensional network arising from the three-pronged quaternary alkene linkages. The TEM images of both PLP. $_{\rm NH2}$ and PLP. $_{\rm micro}$ showed nanostructure gullies on the surface (Fig. 2b), suggesting the presence of a microporous structure. Details on the SEM images for the rest of the synthesized PLP are provided in Fig. S2.

Gas adsorption and desorption isotherms as well as the pore size distribution using non-local density functional theory (NLDFT) of various PLP are provided in Fig. S3 and Table S5. Both PLP $_{\rm NH2}$ and PLP $_{\rm micro}$ exhibited a mixture of micro- and mesopores, whereas PLP $_{\rm meso}$ contained only mesopores (Fig. 2c). Although PLP $_{\rm micro}$ and PLP $_{\rm meso}$ were synthesized via the same route, we postulate that PLP $_{\rm micro}$ incorporated some cross-linking features via 1,3-disubstituted enyne head-totail formation [53,54], resulting in hyper-crosslinked polymers with intrinsic micropores. By contrast, due to the lack of cross-linking,

PLP_{-meso} consisted of flat, smooth particles that were mesoporous.

3.2. Transformation of TNT with PCM-like polymers containing different functional group identities and pore characteristics

The effect of PCM surface functional group identities on TNT decay kinetics was evaluated at pH 7 in the presence of four synthesized PLP, namely PLP-OH, PLP-OH/-N+(CH3)3, PLP-NH2, and PLP-N(CH3)2. All four PLP showed high affinities toward TNT. Specifically, > 99% TNT adsorbed onto polymers within a few minutes (data not shown), suggesting that mass transfer of TNT from the aqueous to the solid phase was not ratelimiting. We analyzed the total mass of TNT from both the aqueous and solid phases over the experimental time frame, so the decay curves in Fig. 3a reflect the decay of the total TNT present in the vial. No TNT decay, nor nitrite production, occurred in 24 h with the PLP containing no functionalities (synthesis details in [38]) or by the synthesis catalyst (palladium) alone (Fig. S4). By contrast, functionalization promoted TNT decay except for the introduction of -N(CH₃)₂ groups. The observed pseudo-first-order rate constants (k_{obs}) for TNT decay followed the order: PLP_{-OH/-N+(CH3)3} ((8.6 \pm 0.4)× 10⁻³ h⁻¹) > PLP_{-NH2} ((4.6 \pm 0.4)× 10⁻³ h⁻¹) > PLP_{-OH} ((2.2 \pm 0.3)× 10⁻³ h⁻¹) > PLP_{-N(CH3)2} (not reactive within 240 h). Notably, the incorporation of QA groups on PLP_{-OH} significantly increased the reaction rates by approximately four-fold at pH 7 compared to without QA (PLP-OH); see Scheme 1 for synthesis route to obtain PLP-OH/-N+(CH3)3. Interestingly, PLP-OH/-N+(CH3)3 showed the lowest percentage of carbon bonded to -N⁺(CH₃)₃. If we normalize the reaction rates to the percentage of carbon bonded to the surface functional group, incorporation of QA increases the intrinsic reaction rate by approximately 14-fold. We conclude that the effectiveness of the catalyst towards TNT hydrolysis is strongly dependent on the identity of the functional group.

The highest reactivity of PLP-OH/-N+(CH3)3 may be in part attributed to the Coulombic attraction between surface QA groups and OH, which increases the hydroxide ion concentration near the surface and accelerates the alkaline hydrolysis of TNT. If the pH inside the pores is close to that in the bulk solution (pH 7), and if the polymer aryl groups have intrinsic pK_a values close to the respective values in the bulk solution of aniline (p $K_a = 4.6$), phenol (p $K_a = 10.0$), and N,N-dimethylaniline (p K_a = 5.1) [55–57], then the polymer Ar-NH₂, Ar-OH, and Ar-N(CH₃)₂ groups will exist predominantly (>98%) in their neutral form. We hypothesize that -OH, -NH2, and -N(CH3)2 groups can react with TNT via nucleophilic aromatic substitution (S_NAr) proceeding through a σ -complex (Scheme S1). The σ -complex is formed by the reversible addition of a nucleophile onto an electron-deficient aromatic carbon. subsequently expelling a leaving group from the same carbon [58]. Thus, the greater reactivity of PLP-NH2 relative to PLP-OH can be explained in terms of basicity and nucleophilicity; Ar-NH2 is a stronger base and more reactive nucleophile than Ar-OH [59,60]. Moreover, several studies found that the deprotonation of the zwitterionic

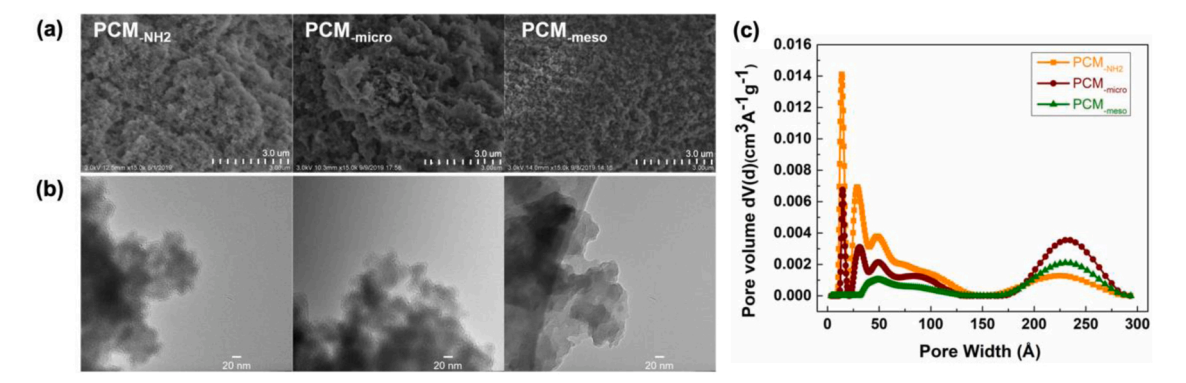


Fig. 2. (a) SEM and (b) TEM images of PLP_{-NH2}, PLP_{-micro}, and PLP_{-meso} calculated from adsorption isotherms using the NL-DFT method.

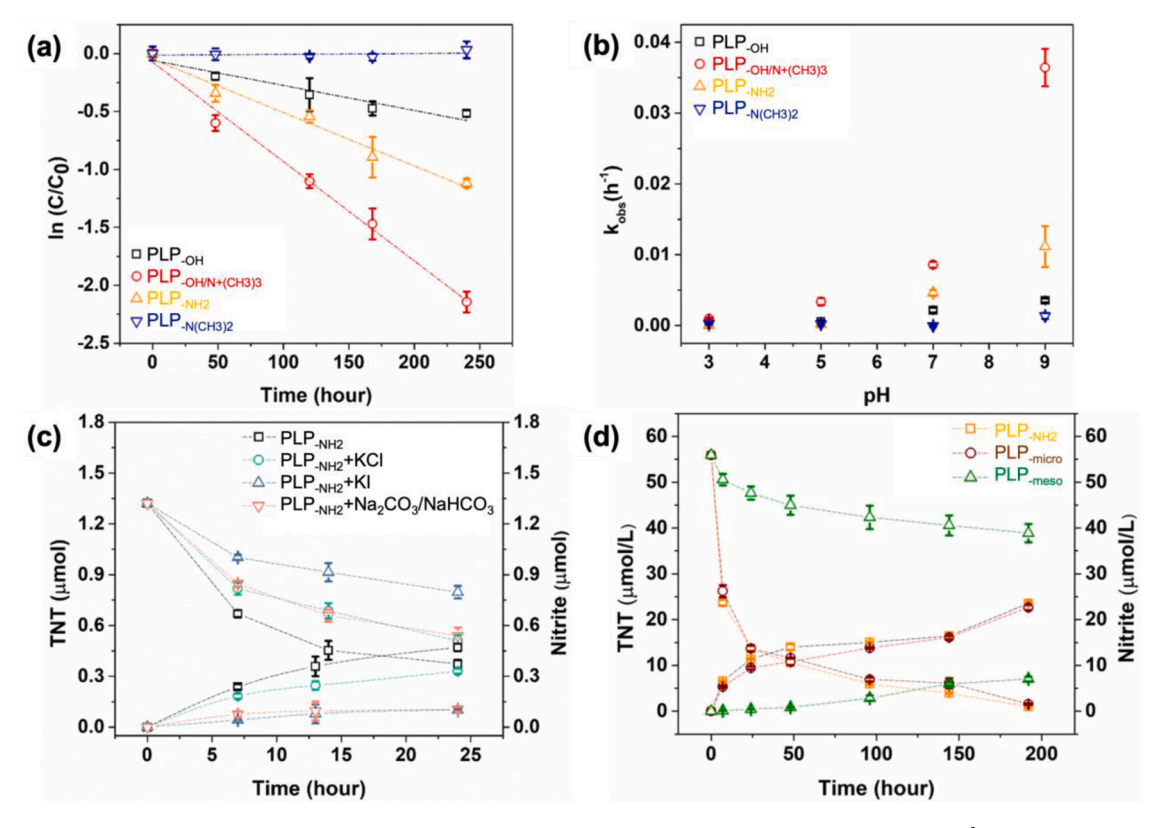


Fig. 3. (a) TNT degradation in the presence of PLP_{-OH} (\square), PLP_{-OH/-N+(CH3)3} (\bigcirc), PLP_{-NH2} (\triangle), and PLP_{-N(CH3)2} (∇) (2.5 g·L⁻¹) at pH 7; (b) The observed pseudo first-order rate constants for TNT decay over pH 3–9 in the presence of PLP_{-OH} (\square), PLP_{-OH/-N+(CH3)3} (\bigcirc), PLP_{-NH2} (\triangle), and PLP_{-N(CH3)2} (∇) (2.5 g·L⁻¹); (c) TNT degradation and nitrite formation in the presence of PLP_{-NH2} (2.5 g•L⁻¹) at pH 9 with or without (\square) the addition of 20 mM of KCl (\bigcirc), KI (\triangle), or Na₂CO₃/NaHCO₃ (∇); (d) TNT degradation and nitrite formation in the presence of PLP_{-NH2} (\square), PLP_{-micro} (\bigcirc), and PLP_{-meso} (\triangle) (2.5 g•L⁻¹) at pH 9. All error bars represent the standard deviation of experimental duplicates.

intermediate (the σ-complex formed between aniline and TNT, Scheme S1) can be assisted by OH [61,62], which is anticipated to be present at higher concentrations in pores and thus may contribute to the higher reactivity of PLP-NH2 in comparison with PLP-OH. The same reaction pathway may also be important for PLP-OH/-N+(CH3)3 due to the presence of Ar-OH groups. Although Ar-N(CH₃)₂ is a stronger base relative to Ar-NH2, we postulate that steric hindrance imparted by the methyl groups of Ar-N(CH₃)₂ could account for the observed lower reactivity of PLP-N(CH3)2 in forming a σ -complex with TNT [63,64]. Similar observations were made previously [65], where phenyl 2,4,6-trinitrophenyl ether reacted much slower with N-methylaniline compared to aniline due to steric crowding at the reaction center. It is likely that an additional methyl group on aniline would slow down the reaction even further. For TNT, however, the methyl group is a poor leaving group so the σ-complex may not ultimately be stable. Furthermore, OH can directly attack TNT via three pathways (Scheme S2) [58,66,67]: (1) nucleophilic aromatic addition by OH⁻ to form a Meisenheimer complex, (2) nucleophilic aromatic substitution by OH to generate dinitro-ortho-cresol and nitrite, and (3) proton abstraction of TNT methyl group yielding the Janovsky complex. A Meisenheimer complex is observed from the formation of a relatively stable intermediate due to the attack of a hydroxyl ion at the C1 or C3 position of TNT in the presence of electron-withdrawing groups and poor leaving groups on the carbon ring [25,58]. Conversely, the Janovsky complex arises from the deprotonation of TNT to form a 2,4,6-trinitrobenzyl anion (TNT') followed by a reaction with a second TNT molecule [58,68].

In addition to nitrite, we detected several organic transformation products in the solid-phase extracts of PLP_{-NH2} using UPLC-qTOF-MS. The relative abundance of TNT ([M-H] $^-$, m/z 226.01, retention time (RT) of 4.34 min) decreased over time in all samples (Fig. S5).

Meanwhile, peak #1 (RT of 2.24 min) was observed after 7 h, the peak intensity of which increased and subsequently decreased after 4 d. Consistent with past studies [58,69], we ascribe peak #1 to a Meisenheimer complex ([M+OH], m/z 244.02). Peak #2 (RT of 3.90 min) appeared after 2 d (Fig. S5) and may be ascribed to 2-amino-4, – 6-dinitrotoluene (M-2 O+H, m/z 196.04). We speculate that this product could be formed by the reduction of a TNT hydrolysis intermediate by PLP, which was shown to have intrinsic reducing capacity in our previous work [38]. Peak #3 (RT of 4.52 min) was observed after 4 d and has a mass spectral signature ([M+M-H], m/z 453.16) consistent with the postulated proton abstraction pathway and subsequent formation of a Janovsky complex.

Although we looked for dinitro-ortho-cresol that may be formed by OH replacing a nitro group of TNT ([M-NO], m/z 197.02), we did not detect such a product by UPLC-qTOF-MS. Nonetheless, our results suggest that TNT hydrolysis can be catalyzed by PLP via either (1) base catalysis involving surface functional groups, which serve as weak bases via S_N Ar pathway with the formation of a σ -complex, and/or (2) reaction with OH where the local pH inside of the pores was enhanced by PLP. The possible reaction pathways are summarized in Scheme S1 and S2. Notably, the first mechanism predicts poisoning of the PLP by the σ -complexes where TNT is covalently bound to the PLP surfaces. Previous studies predicted that the formation of a Meisenheimer complex and proton abstraction were two favorable pathways for TNT base hydrolysis in the absence of solids [58,66,67]. For the first time, we report that two additional pathways are possible in the presence of PLP, namely, the S_NAr involving OH⁻ (aq) or S_NAr involving surface functional groups such as -OH and -NH2. We postulate that PLP could help stabilize reaction intermediates, such as the Meisenheimer complex and Janovsky complex, and thus accelerate the reaction in the

heterogeneous system.

To further interrogate the mechanistic hypotheses, we evaluated the effect of pH on TNT decay $k_{\rm obs}$ over the range of 3–9 (Fig. 3b; corresponding decay curves in Fig. S6). As shown in Fig. 3b, TNT decay was negligible at pH 3 for all PLP. However, as the pH increased $k_{\rm obs}$ increased exponentially in the order: PLP- $_{\rm OH/-N+(CH3)3}$ > PLP- $_{\rm NH2}$ > PLP- $_{\rm OH}$ > PLP- $_{\rm N(CH3)2}$. The $k_{\rm obs}$ for PLP- $_{\rm OH/-N+(CH3)3}$ increased considerably more than the others; for instance, $k_{\rm obs}$ was 4-times greater for PLP- $_{\rm OH/-N+(CH3)3}$ than PLP- $_{\rm OH}$ at pH 7, but 10-times greater at pH 9. Together these results underscore the important role that OH-ion exchange—made possible by the QA group of PLP- $_{\rm OH/-N+(CH3)3}$ —plays in rate enhancement by these polymers.

If OH was able to accumulate at PLP surfaces and thus accelerate TNT decay, we postulated that the addition of anions that compete with OH for anion exchange sites could slow down the reaction. To examine this hypothesis, we chose a series of anions with different charges and sizes (e.g., I, Cl⁻, CO₃²/HCO₃) similar to the competitive adsorption experiments in a previous study [26]. PLP.NH2 was selected as the test polymer to determine whether OH⁻ anion exchange was important also for the behavior of the -NH₂-functionalized polymer. As shown in Fig. 3c, the addition of 20 mM anion regardless of identity slowed down TNT decay, with the order of inhibition relative to the control (no added salt) being, KI > KCl ≈ Na₂CO₃/NaHCO₃. The observed trend can be attributed to a combination of anion size and polarizability, which govern affinity for anion exchange sites on PCM surfaces. For instance, I is much larger and more polarizable than Cl⁻ and can more effectively compete with OH for adsorption sites, thus decreasing the local OH concentrations near PLP surfaces. Similar to a previous study [25], we identified nitrite as a transformation product of TNT hydrolysis, where the decay of 1.35 µmol TNT was observed in concurrence with the formation of 0.45 µmol of nitrite in the presence of PLP-NH2 (Fig. 3c). The molar ratio yield of nitrite to TNT is thus approximately 1:3 for PLP-NH2. The ratio remained between 1:2 and 1:3 for other types of PLPs and PCM, which is similar to what was observed in a previous study [25]. Overall, our results suggest that the denitration pathway occurs (Scheme S2), releasing nitrite. However, since the nitrite yield was lower than the theoretical yield of 1:1, it is likely other reaction pathways such as the formation of Meisenheimer complex or σ -complex also played a key role.

We also evaluated the effect of PCM pore characteristics on TNT decay, where TNT decay rates were monitored in the presence of PLP $_{\rm NH2}$, PLP $_{\rm micro}$, or PLP $_{\rm meso}$. Our previous characterization indicated that PLP $_{\rm NH2}$ and PLP $_{\rm micro}$ both exhibit a mixture of micropores and mesopores, whereas PLP $_{\rm meso}$ contains mesopores exclusively. As shown in Fig. 3d, TNT decay rates followed the trend: PLP $_{\rm NH2} \approx {\rm PLP}_{\rm micro} > {\rm PLP}_{\rm meso}$. The formation of nitrite, again, mirrored the extent of TNT decay: PLP $_{\rm NH2} \approx {\rm PLP}_{\rm micro} > {\rm PLP}_{\rm meso}$. We postulate that the nanopores in PLP $_{\rm NH2}$ and PLP $_{\rm micro}$ could serve as nanoreactors in accelerating TNT hydrolysis. It is possible that the relative locations or orientations of the TNT molecules were altered due to the confinement in these nanopores, which will be verified in the following section using a computational approach.

3.3. Molecular dynamics modeling

Further evidence for the impact of surface groups and confinement on TNT behavior in the nanopores was confirmed by molecular dynamics simulations. Due to statistical requirements, solution concentrations of TNT and NaOH had to be much greater in simulations than in experiments. For example, a single TNT molecule placed in a simulation cell of 2-nm pore size, corresponds to an effective concentration of 0.147 M in the electrolyte, which significantly exceeds the concentrations used in the kinetics experiments. However, as pointed out by Yang et al. [70,71], while the use of high concentrations is likely to accelerate aggregation of TNT molecules, it is unlikely to significantly alter the general structure. In all our simulations, the addition of TNT resulted in TNT aggregation both at the graphene surface and in the interstitial

water phase of the nanopore (Figs. S7 and S8). For plain graphene surfaces (Figs. S7a and S8a), TNT was observed to consistently lie flat on the carbon sheet to minimize interaction with the water phase. As the pore size increased and more TNT was added, the molecules quickly formed aggregates that either spanned the opposing graphene sheets for very small pore separations (1-2 nm), or formed layered structures on the sheets for larger separations. The favoring of surface adsorption and aggregate formation was further verified by annealing simulations (not shown), in which the temperature of the electrolyte was raised by 50 °C and then cooled back to room temperature. The pre- and post-annealed structures showed similar adsorption and aggregation geometries. Hence, it is clear that the molecular dynamics simulations show preferential adsorption of the TNT to the plain carbon surface and aggregation at locally high concentrations. Further, these simulations demonstrate that it is plausible that pore size impacts TNT orientations (from bridging at 1-2 nm interplanar separations to sticking to one surface for larger separations) that could affect its reactivity toward OH.

Upon introduction of positively charged QA groups, the structure changes dramatically at the PCM interface. As the number of surface groups increases, the resulting density of OH- at the graphite surface increases by a factor of four relative to the density in the middle of the pore (Fig. 5). Hence, the impact of the surface-bound cations is to attract OH in competition with the neutralizing Cl included at the onset of the simulation. In addition to driving the accumulation of OH and Cl, the surface QA groups also impact the distribution of TNT in the pore. At low QA surface coverage, TNT still seeks to adsorb on the exposed graphene. However, at sufficiently high QA surface coverage, TNT is blocked from lying flat on the graphene sheet and instead aggregates in the fluid away from the pore wall (Figs. 4, S7–S10, Table S6). The observation of these TNT surface layering at intermediate charge densities is intriguing because it demonstrates collection of TNT molecules close to the surface in the same spatial region where hydroxide is likewise accumulating relative to its concentration in the interstitial fluid. Hence, we see evidence from the molecular dynamics simulations that the presence of the surface groups can play a role in accelerating TNT hydrolysis by acting to concentrate both TNT and hydroxide near the pore wall.

3.4. PCM types and stability

To translate the knowledge gained from the PLP, TNT decay was investigated with commercially available, powdered AC (Norit D10, Norit_RO) and PAC modified with QA groups (Norit_RO_PD) at pH 10. The solid phase extraction efficiencies for TNT from Norit D10, Norit_RO, and Norit_RO_PD were 71%, 21%, and 27%, respectively. This may be compared to more than 99% for graphite [25]. As shown in Fig. 5a and b, TNT exhibited faster decay in samples containing Norit RO PD than Norit RO, with an estimated half-life of 0.2 d and 1 d, respectively. Consistent with results from PLP, nitrite was observed as one of the transformation products, where approximately 0.033 µmol nitrite formed in the presence of Norit RO PD, while only 0.015 µmol nitrite formed in the presence of Norit RO. These values correspond to nitrite:TNT molar ratios of approximately 1:1.5 and 1:3.3, respectively. Over 99% of nitrite was observed in the aqueous phase. Neither TNT decay nor nitrite formation was observed in the controls, with or without PAC, at pH 3. No TNT decay was observed at pH 10 in the absence of PAC even after 4 days (data not shown). Our results suggest that by simply non-covalently adsorbing QA polymers onto PCM, the reactivity of PCM can be doubled, possibly due to an enhanced local pH near PCM surfaces [19,26].

Formation of a σ -complex or other poorly-reversible covalently-bound TNT complex to the catalyst could result in catalyst poisoning. To determine whether catalyst poisoning occurred during the reaction, TNT hydrolysis and nitrite formation with and without PAC (Norit D10) was monitored at pH 10 with 10 successive additions of TNT. We chose a TNT-to-PAC ratio of 100 μ mol·g $^{-1}$ to ensure that TNT was in abundance relative to the reactive sites of PAC. The reported PAC anion-exchange

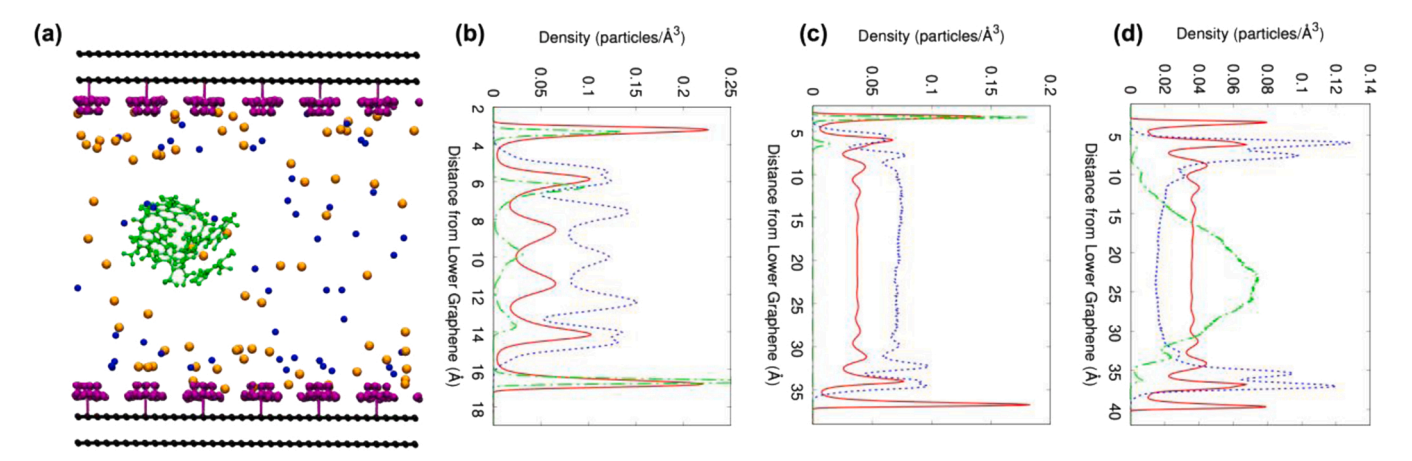


Fig. 4. (a) Ball-and-stick model of TNT confined between four layers of graphene with quaternary ammonium groups with a 4-nm distance, black = graphite, green = TNT, purple = ammonium groups, orange = chloride ions, blue = hydroxide oxygen. Density profiles are also shown for water molecules (red solid), hydroxide ions (blue dotted), and the TNT nitrogen (green dot-dashed) confined between plain graphene sheets (b) 2-nm apart and (c) 4-nm apart. For comparison, the same density profiles are shown in (d) for the 4-nm wide pore decorated with ammonium groups in (a).

capacity (AEC) (i.e., $113.7 \pm 0.6 \, \mu \text{mol} \cdot \text{g}^{-1}$ [26]) was used to estimate the reactive sites of PAC due to their critical role in accumulating OHand facilitating base hydrolysis. To speed up the experiments and make a longer period of evaluation possible, we performed the experiments at 55 °C. This temperature also allows us to understand the stability of the catalyst at an elevated temperature, which could be of relevance to conditions in engineering reactors. As shown in Fig. 5c, both nitrite formation and TNT decay were observed at a nitrite:TNT molar ratio of approximately 1:3 for the first seven cycles, which is consistent with the PLP work. A slight decrease (~10%) in the amount of TNT decay and nitrite formation in the last three cycles (Cycles 8-10) were observed. Neither TNT decay nor nitrite formation was observed in controls containing TNT in 10 mM citrate buffer (pH 3.0 \pm 0.2) with/without PAC (data not shown). We hypothesize that the observed decline in PAC performance was due to the formation of σ -complex between TNT and surface functional groups (e.g., -NH₂ or -OH), resulting in the irreversible binding of TNT and blockage of the adsorption sites. We also quantified surface functional groups of pristine and used PAC (Norit D10) using XPS. The XPS survey of both pristine and used PAC confirms the presence of elemental O, N, and C, which corresponds to binding energies of 532.8, 399.2, and 284.8 eV, respectively (Fig. S11a) [72-77]. The amount of elemental O increased slightly from the pristine PAC to the used PAC. By employing peak deconvolution in the C 1s spectra, we were able to quantify the amount of C-OH and C-N surface functional groups in both pristine and used PAC, which are 22.0% and 18.9% as well as 9.5% and 9.7%, respectively (Fig. S11b). These results suggest negligible changes in surface functional groups (e.g., C-OH and C-N) following TNT hydrolysis. Similar trends were observed for -OH and C=O by deconvoluting the O 1s spectra (Fig. S11c). Overall, our XPS results further support that the PAC surface functional groups are relatively stable, where no significant changes in the O- and N-functional groups were observed during TNT transformation.

4. Conclusions

We showed that -OH and -NH $_2$ functional groups can serve as weak bases to facilitate TNT hydrolysis, whereas -N(CH $_3$) $_3^+$ groups can increase the local pH by accumulating OH $^-$ near PCM surfaces. Moreover, the micropores of PCM seem capable of altering the chemical environment around TNT molecules (including its location and orientation) in such a way as to facilitate its hydrolysis. Our study is the first attempt to scrutinize the complex properties of PCM that promote surface hydrolysis, namely the functional group identity and pore characteristics. The findings of this study have broad implications for the field of catalysis

and environmental engineering. Firstly, our results that PCM functional groups promoted TNT hydrolysis via two distinctive reaction mechanisms, namely direct base catalysis vs. OH- accumulation near surfaces, provide critical guidance for engineering highly reactive materials. For instance, the formation of σ -complexes between -NH₂ surface functional groups and TNT suggests that PCM rich in -NH2 functional groups could be easily poisoned due to irreversible TNT binding, which was supported by the slight decrease in PAC performance in our results from the 10 successive additions of TNT. By contrast, -N(CH₃)₃⁺ functional groups could adsorb TNT while simultaneously facilitating its transformation. Thus, efforts can be directed to populate selected functional groups on carbon amendments for groundwater and soil remediation, for instance, increase the abundance of QA groups while decreasing the presence of -NH₂ and -OH, which can reduce the need for PCM regeneration given that contaminants will be destroyed on PCM surfaces rather than filling up adsorption sites.

Secondly, this is the first study using a combined experimental and computational approach to demonstrate that surface OA groups can effectively attract OH and thereby increase the local OH concentration near the PCM surface. This finding has implications over the adsorbent design for removing anionic pollutants, including nitrate, phosphate, and anionic per- and polyfluoroalkyl substances (PFAS) [78,79]. It is likely that the surface properties of PCM can be tailored to better retain these anionic pollutants similarly as OH. This topic should be further studied. Lastly, our findings that the confinement of TNT in PCM micropores enables a reaction pathway that otherwise would not occur under the pH conditions (i.e., circumneutral to 10) provide insights on alternative synthesis approaches that are 'greener' for the field of catalysis and drug delivery. For instance, the potential use of such nanoreactors could allow reactions to proceed in water without using organic solvents that are often toxic and hazardous while maintaining high yield and selectivity [37,80,81].

CRediT authorship contribution statement

Zhao Li: Data curation, Formal analysis, Methodology, Writing – original draft. Ryan Jorn: Data curation, Formal analysis, Methodology. Pamela Rose V. Samonte: Data curation, Formal analysis, Writing – review & editing. Jingdong Mao: Data curation, Formal analysis, Writing – review & editing. John D. Sivey: Formal analysis, Writing – review & editing. Joseph J. Pignatello: Formal analysis, Writing – review & editing. Wenqing Xu: Project administration, Formal analysis, Supervision, Writing – original draft, Writing – review & editing.

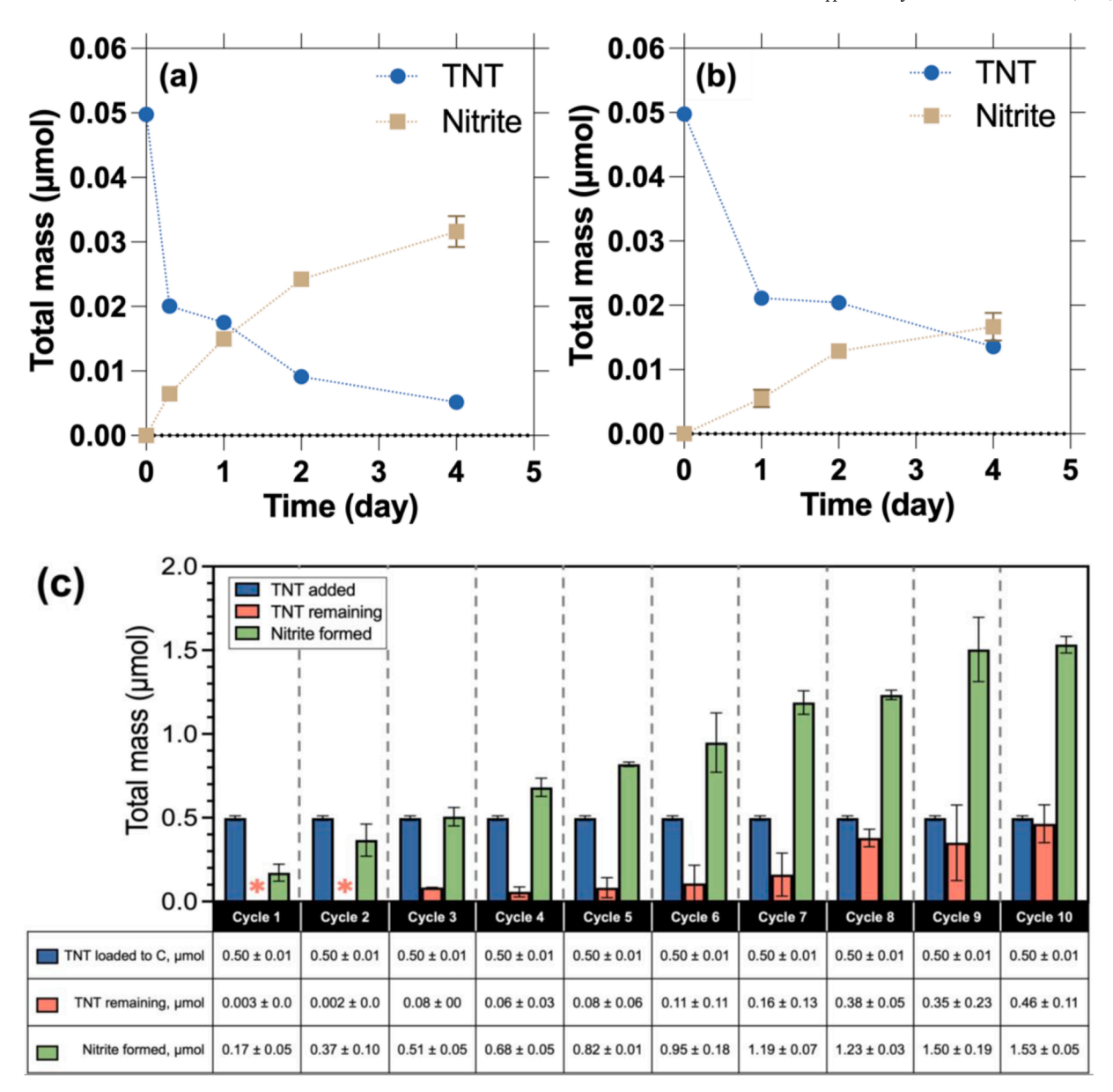


Fig. 5. Disappearance of TNT and detection of nitrite at pH 10 in the presence of (a) Norit_RO_PD and (b) Norit_RO. Uniform conditions: $[TNT]_0 = 0.05 \,\mu\text{mol}$, $[PAC] = 10 \,\,\text{g}\cdot\text{L}^{-1}$, $T = 25 \,\,^{\circ}\text{C}$, pH = 10.2 (10 mM carbonate buffer); controls without PCM were simultaneously performed at pH 10 (10 mM carbonate buffer) and with/without PCM at pH 3.1 (10 mM citrate buffer). (c) TNT hydrolysis and nitrite formation with and without Norit D10 over 10 days with 10 successive additions of TNT. Each time, $0.5 \,\mu\text{mol}$ of TNT was loaded to the system. The remaining TNT and nitrite formation were measured after 1 day for 10 times (i.e., Cycles 1, 2, 3, 4, 5, 6, 7, 8, 9, 10). Orange asterisk (*) represents values that are far below the present scale. Uniform conditions: $[TNT]_0 = 0.5 \,\mu\text{mol}$, $[PAC] = 2.5 \,\,\text{g}\cdot\text{L}^{-1}$, $T = 55 \,\,^{\circ}\text{C}$, pH = 10.2 (10 mM carbonate buffer); controls without PCM were simultaneously performed at pH 10 (10 mM carbonate buffer). Error bars represent the standard deviation of duplicate samples.

Declaration of Competing Interest

The authors declare that they have no known competing financial interests or personal relationships that could have appeared to influence the work reported in this paper.

Data availability

Data will be made available on request.

Acknowledgments

W.X. and Z.L. acknowledge the U.S. National Science Foundation CAREER award (CBET-1752220) for the financial support. W.X and J.J.P.

acknowledge support by the U.S. Department of Defense through the Strategic Environmental Research and Development Program (SERDP ER19-1239). W.X. acknowledges support from the National Institutes of Health award (1R01ES032671-01). Z.L., P.R.V.S., and W.X. would also like to acknowledge Xiaolei Xu for assistance in running several experiments, Drs. Michael Smith and Charles Coe at Villanova University for their help with the BET surface measurements, Dr. Walter Boyko at Villanova University for his help with the FTIR measurement, Dr. Gang Feng at Villanova University for his assistance with the SEM images, and Dr. Dmitri Barbash at Materials Characterization Core Facilities at Drexel University for assistance with the XPS images. All simulations were run on the Augie High Performance Computing cluster, funded by NSF award 2018933, at Villanova University. J.D.S. acknowledges funding from the Henry Dreyfus Teacher-Scholar Awards Program (TH-

20-021). The graphical abstract was created with BioRender.com.

Appendix A. Supplementary material

Supplementary data associated with this article can be found in the online version at doi:10.1016/j.apcatb.2022.121877.

References

- J. Pignatello, W.A. Mitch, W. Xu, Activity and reactivity of pyrogenic carbonaceous matter toward organic compounds, Environ. Sci. Technol. 51 (2017) 8893–8908.
- [2] W. Xu, M.L. Segall, Z. Li, Reactivity of pyrogenic carbonaceous matter (PCM) in mediating environmental reactions: current knowledge and future trends, Front. Environ. Sci. Eng. 14 (2020) 1–11.
- [3] Y.-M. Cho, U. Ghosh, A.J. Kennedy, A. Grossman, G. Ray, J.E. Tomaszewski, D. W. Smithenry, T.S. Bridges, R.G. Luthy, Field application of activated carbon amendment for in-situ stabilization of polychlorinated biphenyls in marine sediment, Environ. Sci. Technol. 43 (2009) 3815–3823.
- [4] M.T. Jonker, A.A. Koelmans, Sorption of polycyclic aromatic hydrocarbons and polychlorinated biphenyls to soot and soot-like materials in the aqueous environment: mechanistic considerations, Environ. Sci. Technol. 36 (2002) 3275–3734
- [5] U. Ghosh, R.G. Luthy, G. Cornelissen, D. Werner, C.A. Menzie, In-situ sorbent amendments: a new direction in contaminated sediment management, Environ. Sci. Technol. 45 (2011) 1163–1168.
- [6] A.A. Koelmans, M.T. Jonker, G. Cornelissen, T.D. Bucheli, P.C. Van Noort, Ö. Gustafsson, Black carbon: the reverse of its dark side, Chemosphere 63 (2006) 365–377.
- [7] R.G. Luthy, G.R. Aiken, M.L. Brusseau, S.D. Cunningham, P.M. Gschwend, J. J. Pignatello, M. Reinhard, S.J. Traina, W.J. Weber, J.C. Westall, Sequestration of hydrophobic organic contaminants by geosorbents, Environ. Sci. Technol. 31 (1997) 3341–3347.
- [8] J.A. Simon, Editor's Perspective—An in Situ Revelation: First Retard Migration, Then Treat, Remediation, 2015.
- [9] R.B. Payne, U. Ghosh, H.D. May, C.W. Marshall, K.R. Sowers, A pilot-scale field study: in situ treatment of PCB-impacted sediments with bioamended activated carbon, Environ. Sci. Technol. 53 (2019) 2626–2634.
- [10] P. Oleszczuk, P. Godlewska, D.D. Reible, P. Kraska, Bioaccessibility of polycyclic aromatic hydrocarbons in activated carbon or biochar amended vegetated (Salix viminalis) soil, Environ. Pollut. 227 (2017) 406–413.
- [11] C.R. Patmont, U. Ghosh, P. LaRosa, C.A. Menzie, R.G. Luthy, M.S. Greenberg, G. Cornelissen, E. Eek, J. Collins, J. Hull, In situ sediment treatment using activated carbon: a demonstrated sediment cleanup technology, Integr. Environ. Assess. Manag. 11 (2015) 195–207.
- [12] J. Renholds, In Situ Treatment of Contaminated Sediments, 1998.
- [13] M. Cayuela, L. Van Zwieten, B. Singh, S. Jeffery, A. Roig, M. Sánchez-Monedero, Biochar's role in mitigating soil nitrous oxide emissions: a review and metaanalysis, Agric. Ecosyst. Environ. 191 (2014) 5–16.
- [14] J. Lehmann, M.C. Rillig, J. Thies, C.A. Masiello, W.C. Hockaday, D. Crowley, Biochar effects on soil biota—a review, Soil Biol. Biochem. 43 (2011) 1812–1836.
- [15] J.M. Kemper, E. Ammar, W.A. Mitch, Abiotic degradation of hexahydro-1, 3, 5-trinitro-1, 3, 5-triazine in the presence of hydrogen sulfide and black carbon, Environ. Sci. Technol. 42 (2008) 2118–2123.
- [16] S.-Y. Oh, J.-G. Son, P.C. Chiu, Black carbon-mediated reductive transformation of nitro compounds by hydrogen sulfide, Environ. Earth Sci. 73 (2015) 1813–1822.
- [17] W. Xu, K.E. Dana, W.A. Mitch, Black carbon-mediated destruction of nitroglycerin and RDX by hydrogen sulfide, Environ. Sci. Technol. 44 (2010) 6409–6415.
- [18] W. Xu, J.J. Pignatello, W.A. Mitch, Role of black carbon electrical conductivity in mediating hexahydro-1, 3, 5-trinitro-1, 3, 5-triazine (RDX) transformation on carbon surfaces by sulfides, Environ. Sci. Technol. 47 (2013) 7129–7136.
- [19] H.-S. Hsieh, J.J. Pignatello, Activated carbon-mediated base hydrolysis of alkyl bromides, Appl. Catal. B Environ. 211 (2017) 68–78.
- [20] K.S. Sing, Reporting physisorption data for gas/solid systems with special reference to the determination of surface area and porosity (Recommendations 1984), Pure Appl. Chem. 57 (1985) 603–619.
- [21] J.H. Atkins, Porosity and surface area of carbon black, Carbon 3 (1965) 299–303.
- [22] V.L. Snoeyink, W.J. Weber, The surface chemistry of active carbon; a discussion of structure and surface functional groups, Environ. Sci. Technol. 1 (1967) 228–234.
- [23] K. Mackenzie, J. Battke, R. Koehler, F.-D. Kopinke, Catalytic effects of activated carbon on hydrolysis reactions of chlorinated organic compounds: part 2. 1, 1, 2, 2tetrachloroethane, Appl. Catal. B Environ. 59 (2005) 171–179.
- [24] W. Chen, D. Zhu, S. Zheng, W. Chen, Catalytic effects of functionalized carbon nanotubes on dehydrochlorination of 1, 1, 2, 2-tetrachloroethane, Environ. Sci. Technol. 48 (2014) 3856–3863.
- [25] K. Ding, C. Byrnes, J. Bridge, A. Grannas, W. Xu, Surface-promoted hydrolysis of 2,4,6-trinitrotoluene and 2,4-dinitroanisole on pyrogenic carbonaceous matter, Chemosphere 197 (2018) 603–610.
- [26] H.-S. Hsieh, J.J. Pignatello, Modified carbons for enhanced nucleophilic substitution reactions of adsorbed methyl bromide, Appl. Catal. B Environ. 233 (2018) 281–288.
- [27] R. Zangi, J.B. Engberts, Physisorption of hydroxide ions from aqueous solution to a hydrophobic surface, J. Am. Chem. Soc. 127 (2005) 2272–2276.

- [28] D.J. Cole, P.K. Ang, K.P. Loh, Ion adsorption at the graphene/electrolyte interface, J. Phys. Chem. Lett. 2 (2011) 1799–1803.
- [29] X. Liu, L. Dai, Carbon-based metal-free catalysts, Nat. Rev. Mater. 1 (2016) 1-12.
- [30] V. Pascanu, G. González Miera, A.K. Inge, Bn Martín-Matute, Metal-organic frameworks as catalysts for organic synthesis: a critical perspective, J. Am. Chem. Soc. 141 (2019) 7223–7234.
- [31] A.B. Grommet, M. Feller, R. Klajn, Chemical reactivity under nanoconfinement, Nat. Nanotechnol. 15 (2020) 256–271.
- [32] Y. Shichida, T. Matsuyama, Evolution of opsins and phototransduction, Philos. Trans. R. Soc. B Biol. Sci. 364 (2009) 2881–2895.
- [33] H. Wang, Y. Wang, B. Shen, X. Liu, M. Lee, Substrate-driven transient self-assembly and spontaneous disassembly directed by chemical reaction with product release, J. Am. Chem. Soc. 141 (2019) 4182–4185.
- [34] E. Castillejos, P.J. Debouttière, L. Roiban, A. Solhy, V. Martinez, Y. Kihn, O. Ersen, K. Philippot, B. Chaudret, P. Serp, An efficient strategy to drive nanoparticles into carbon nanotubes and the remarkable effect of confinement on their catalytic performance, Angew. Chem. Int. Ed. 48 (2009) 2529–2533.
- [35] J. Xiao, X. Pan, S. Guo, P. Ren, X. Bao, Toward fundamentals of confined catalysis in carbon nanotubes, J. Am. Chem. Soc. 137 (2015) 477–482.
- [36] Y. Kohyama, T. Murase, M. Fujita, Metal-organic proximity in a synthetic pocket, J. Am. Chem. Soc. 136 (2014) 2966–2969.
- [37] S. Zhang, T. Hedtke, L. Wang, X. Wang, T. Cao, M. Elimelech, J.-H. Kim, Engineered nanoconfinement accelerating spontaneous manganese-catalyzed degradation of organic contaminants, Environ. Sci. Technol. (2021).
- [38] Z. Li, J. Mao, W. Chu, W. Xu, Probing the surface reactivity of pyrogenic carbonaceous material (PCM) through synthesis of PCM-like conjugated microporous polymers, Environ. Sci. Technol. 53 (2019) 7673–7682.
- [39] J.-X. Jiang, F. Su, A. Trewin, C.D. Wood, H. Niu, J.T. Jones, Y.Z. Khimyak, A. I. Cooper, Synthetic control of the pore dimension and surface area in conjugated microporous polymer and copolymer networks, J. Am. Chem. Soc. 130 (2008) 7710–7720.
- [40] R. Dawson, A. Laybourn, R. Clowes, Y.Z. Khimyak, D.J. Adams, A.I. Cooper, Functionalized conjugated microporous polymers, Macromolecules 42 (2009) 8809–8816.
- [41] J.-H. Li, Y. Liang, Y.-X. Xie, Efficient palladium-catalyzed homocoupling reaction and Sonogashira cross-coupling reaction of terminal alkynes under aerobic conditions, J. Org. Chem. 70 (2005) 4393–4396.
- [42] R.L. Johnson, K. Schmidt-Rohr, Quantitative solid-state ¹³C NMR with signal enhancement by multiple cross polarization, J. Magn. Reson. 239 (2014) 44–49.
- [43] X.-P. Tang, A. Kleinhammes, H. Shimoda, L. Fleming, K. Bennoune, S. Sinha, C. Bower, O. Zhou, Y. Wu, Electronic structures of single-walled carbon nanotubes determined by NMR, Science 288 (2000) 492–494.
- [44] J.-D. Mao, K. Schmidt-Rohr, Recoupled long-range C-H dipolar dephasing in solidstate NMR, and its use for spectral selection of fused aromatic rings, J. Magn. Reson. 162 (2003) 217–227.
- [45] H.J.C. Berendsen, J.R. Grigera, T.P. Straatsma, The missing term in effective pair potentials, J. Phys. Chem. 91 (1987) 6269–6271.
- [46] D.J. Bonthuis, S.I. Mamatkulov, R.R. Netz, Optimization of classical nonpolarizable force fields for OH(-) and H3O(+), J. Chem. Phys. 144 (2016), 104503.
- [47] P. Dauber-Osguthorpe, V.A. Roberts, D.J. Osguthorpe, J. Wolff, M. Genest, A. T. Hagler, Structure and energetics of ligand binding to proteins: Escherichia coli dihydrofolate reductase-trimethoprim, a drug-receptor system, Proteins 4 (1988) 31-47
- [48] L. Martínez, R. Andrade, E.G. Birgin, J.M. Martínez, PACKMOL: a package for building initial configurations for molecular dynamics simulations, J. Comput. Chem. 30 (2009) 2157–2164.
- [49] S. Plimpton, Fast parallel algorithms for short-range molecular dynamics, J. Comput. Phys. 117 (1995) 1–19.
- [50] E. Pretsch, P. Bühlmann, C. Affolter, E. Pretsch, P. Bhuhlmann, C. Affolter. Structure Determination Of Organic Compounds, 2000.
- [51] M. Domingo-Garcia, I. Fernandez-Morales, F.J. Lopez-Garzon, C. Moreno-Castilla, Determination of the micropore texture of some glassy carbons using molecular probes, Langmuir (1997) 1218–1224.
- [52] G. Marcelin, P.R. Brooks, Steric hindrance in potassium atom-oriented molecule reactions. Methyl iodide and tert-butyl iodide, J. Am. Chem. Soc. 97 (1975) 1710–1715.
- [53] A.S. Batsanov, J.C. Collings, I.J. Fairlamb, J.P. Holland, J.A. Howard, Z. Lin, T. B. Marder, A.C. Parsons, R.M. Ward, J. Zhu, Requirement for an oxidant in Pd/Cu co-catalyzed terminal alkyne homocoupling to give symmetrical 1, 4-disubstituted 1, 3-diynes, J. Org. Chem. 70 (2005) 703–706.
- [54] J.-X. Jiang, F. Su, H. Niu, C.D. Wood, N.L. Campbell, Y.Z. Khimyak, A.I. Cooper, Conjugated microporous poly (phenylene butadiynylene) s, Chem. Commun. (2008) 486–488.
- [55] CRC Handbook of Chemistry and Physics, 2009–2010, 90th ed., J. Am. Chem. Soc., 131, 2009, pp. 12862–12862.
- [56] U. Chaudry, P. Popelier, Estimation of p K a using quantum topological molecular similarity descriptors: application to carboxylic acids, anilines and phenols, J. Org. Chem. 69 (2004) 233–241.
- [57] K.C. Gross, P.G. Seybold, Z. Peralta-Inga, J.S. Murray, P. Politzer, Comparison of quantum chemical parameters and Hammett constants in correlating p K a values of substituted anilines, J. Org. Chem. 66 (2001) 6919–6925.
- [58] A.J. Salter-Blanc, E.J. Bylaska, J.J. Ritchie, P.G. Tratnyek, Mechanisms and kinetics of alkaline hydrolysis of the energetic nitroaromatic compounds 2,4,6-trinitrotoluene (TNT) and 2,4-dinitroanisole (DNAN), Environ. Sci. Technol. 47 (2013) 6790–6798.

- [59] A. Kütt, V. Movchun, T. Rodima, T. Dansauer, E.B. Rusanov, I. Leito, I. Kaljurand, J. Koppel, V. Pihl, I. Koppel, G. Ovsjannikov, L. Toom, M. Mishima, M. Medebielle, E. Lork, G.-V. Röschenthaler, I.A. Koppel, A.A. Kolomeitsev, Pentakis (trifluoromethyl)phenyl, a sterically crowded and electron-withdrawing group: synthesis and acidity of pentakis(trifluoromethyl)benzene, -toluene, -phenol, and -aniline, J. Org, Chem. 73 (2008) 2607–2620.
- [60] D. Shao, J. Hu, C. Chen, G. Sheng, X. Ren, X. Wang, Polyaniline multiwalled carbon nanotube magnetic composite prepared by plasma-induced graft technique and its application for removal of aniline and phenol, J. Phys. Chem. C 114 (2010) 21524–21530.
- [61] E. Buncel, W. Eggimann, Base catalysis of sigma.-complex formation between 1,3,5-trinitrobenzene and aniline in dimethyl sulfoxide. Rate limiting proton transfer, J. Am. Chem. Soc. 99 (1977) 5958–5964.
- [62] G.A. Artamkina, M.P. Egorov, I.P. Beletskaya, Some aspects of anionic.sigma.complexes, Chem. Rev. 82 (1982) 427–459.
- [63] H. Wu, T. Zhao, X. Hu, Friedel-Crafts reaction of N,N-dimethylaniline with alkenes catalyzed by cyclic diaminocarbene-gold(I) complex, Sci. Rep. 8 (2018) 11449.
- [64] A. Kanavarioti, M.W. Stronach, R.J. Ketner, T.B. Hurley, Large steric effect in the substitution reaction of amines with phosphoimidazolide-activated nucleosides, J. Org. Chem. 60 (1995) 632–637.
- [65] M.R. Crampton, T.A. Emokpae, J.A.K. Howard, C. Isanbor, R. Mondal, Leaving group effects on the mechanism of aromatic nucleophilic substitution (SNAr) reactions of some phenyl 2,4,6-trinitrophenyl ethers with aniline in acetonitrile, J. Phys. Org. Chem. 17 (2004) 65–70.
- [66] F.C. Hill, L.K. Sviatenko, L. Gorb, S.I. Okovytyy, G.S. Blaustein, J. Leszczynski, DFT M06-2X investigation of alkaline hydrolysis of nitroaromatic compounds, Chemosphere 88 (2012) 635–643.
- [67] L. Sviatenko, C. Kinney, L. Gorb, F.C. Hill, A.J. Bednar, S. Okovytyy, J. Leszczynski, Comprehensive investigations of kinetics of alkaline hydrolysis of TNT (2,4,6trinitrotoluene), DNT (2,4-dinitrotoluene), and DNAN (2,4-dinitroanisole), Environ. Sci. Technol. 48 (2014) 10465–10474.
- [68] C.F. Bernasconi, Kinetic and spectral study of some reactions of 2,4,6-trinitrotoluene in basic solution. I. Deprotonation and Janovsky complex formation, J. Org. Chem. 36 (1971) 1671–1679.
- [69] A. Mills, A. Seth, G. Peters, Alkaline hydrolysis of trinitrotoluene, TNT, Phys. Chem. Chem. Phys. 5 (2003) 3921–3927.
- [70] H. Yang, H. Li, L. Liu, Y. Zhou, X. Long, Molecular simulation studies on the interactions of 2,4,6-trinitrotoluene and Its metabolites with lipid membranes, J. Phys. Chem. B 123 (2019) 6481–6491.

- [71] H. Yang, M. Zhou, H. Li, L. Liu, Y. Zhou, X. Long, Collective absorption of 2,4,6-trinitrotoluene into lipid membranes and its effects on bilayer properties. A computational study, RSC Adv. 9 (2019) 39046–39054.
- [72] V. VanDelinder, D.R. Wheeler, L.J. Small, M.T. Brumbach, E.D. Spoerke, I. Henderson, G.D. Bachand, Simple, benign, aqueous-based amination of polycarbonate surfaces, ACS Appl. Mater. Interfaces 7 (2015) 5643–5649.
- [73] L. Zhang, L.-y. Tu, Y. Liang, Q. Chen, Z.-s. Li, C.-h Li, Z.-h. Wang, W. Li, Coconut-based activated carbon fibers for efficient adsorption of various organic dyes, RSC Adv. 8 (2018) 42280–42291.
- [74] A. Castilho Rodrigues-Siqueli, E. Silva, S. Quirino, A. Cuña, J. Marcuzzo, J. Matsushima, E. Gonçalves, M. Baldan, Ag@activated carbon felt composite as electrode for supercapacitors and a study of three different aqueous electrolytes, Mater. Res. 22 (2018).
- [75] W. Dilokekunakul, P. Teerachawanwong, N. Klomkliang, S. Supasitmongkol, S. Chaemchuen, Effects of nitrogen and oxygen functional groups and pore width of activated carbon on carbon dioxide capture: temperature dependence, Chem. Eng. J. 389 (2020), 124413.
- [76] T. Aytug, M.S. Rager, W. Higgins, F.G. Brown, G.M. Veith, C.M. Rouleau, H. Wang, Z.D. Hood, S.M. Mahurin, R.T. Mayes, P.C. Joshi, T. Kuruganti, Vacuum-assisted low-temperature synthesis of reduced graphene oxide thin-film electrodes for high-performance transparent and flexible all-solid-state supercapacitors, ACS Appl. Mater. Interfaces 10 (2018) 11008–11017.
- [77] S. Wang, X. Zhao, T. Cochell, A. Manthiram, Nitrogen-doped carbon nanotube/ graphite felts as advanced electrode materials for vanadium redox flow batteries, J. Phys. Chem. Lett. 3 (2012) 2164–2167.
- [78] C. Ng, I.T. Cousins, J.C. DeWitt, J. Glüge, G. Goldenman, D. Herzke, R. Lohmann, M. Miller, S. Patton, M. Scheringer, X. Trier, Z. Wang, Addressing urgent questions for PFAS in the 21st century, Environ. Sci. Technol. 55 (2021) 12755–12765.
- [79] M.-A. Pétré, D.P. Genereux, L. Koropeckyj-Cox, D.R.U. Knappe, S. Duboscq, T. E. Gilmore, Z.R. Hopkins, Per- and polyfluoroalkyl substance (PFAS) transport from groundwater to streams near a PFAS manufacturing facility in North Carolina, USA, Environ. Sci. Technol. 55 (2021) 5848–5856.
- [80] M.T. De Martino, L.K.E.A. Abdelmohsen, F.P.J.T. Rutjes, J.C.M. van Hest, Nanoreactors for green catalysis, Beilstein J. Org. Chem. 14 (2018) 716–733.
- [81] B.H. Lipshutz, N.A. Isley, J.C. Fennewald, E.D. Slack, On the way towards greener transition-metal-catalyzed processes as quantified by E factors, Angew. Chem. Int. Ed. 52 (2013) 10952–10958.